Assimilation of Simulated Wind Lidar Data with a Kalman Filter

PIERRE GAUTHIER,* PHILIPPE COURTIER, AND PATRICK MOLL

CNRM, Météo-France, Paris, France

(Manuscript received 12 May 1992, in final form 30 November 1992)

ABSTRACT

The object of this paper is to present some results obtained with an extended Kalman filter (EKF). First, a discussion is given of the way that the EKF has been implemented and tested for a global nondivergent barotropic model spectrally truncated at T21. In the present paper, the assimilation experiments focused solely on the time evolution of the forecast error covariances that are influenced by two factors: 1) their time integration performed here with the tangent linear model obtained from a linearization around the true trajectory and 2) the accuracy and distribution of the observations. Data from a simulated radiosonde network have been assimilated over a 24-h period. The results show that even though no model error has been considered, there can be a substantial forecast error growth, especially in regions where the flow is unstable and no data are available. The error growth is attributed to instability processes that are embedded within the complex flow configuration around which the nonlinear model is linearized to obtain the tangent linear model. The impact of different initial conditions for the forecast error covariance is also looked at. In an experiment where the time integration of the forecast error covariance is suppressed, the results show that error growth is suppressed, causing the analysis error variance to differ substantially from the variance field obtained with the EKF. Especially in regions where instability is present and no data are available, this "improved" optimal interpolation considers the forecast to be more accurate than it actually is.

In a second set of experiments, a mini-observing system simulation experiment has been conducted for which wind data from a proposed satellite-based lidar instrument have been simulated and added to the radiosonde data of the previous experiments. Two configurations of the instrument have been considered where the satellite is set on a polar orbit, at an altitude of 400 km in the first scenario and 800 km in the second. Compared to the results obtained with the radiosonde data alone, the global data coverage leads to an improvement in the analysis, especially in the Southern Hemisphere. Data being available in the regions of instability, the assimilation is now capable of putting a stop to the unlimited error growth observed in the previous experiments. Due to a degradation of the measurement when the instrument is at an altitude of 800 km, the analysis is more accurate for the 400-km case, but the low-altitude orbit (400 km) leaves holes in the tropical belt that the data assimilation scheme is not quite able to compensate for.

1. Introduction

Data assimilation can be stated as the determination of the "best estimate" of the state of the atmosphere, given all the available information about the data itself together with a model forecast that encompasses all of our prior knowledge about the atmospheric state. This best estimate can be either one of maximum likelihood (Lorenc 1986, 1988) or one that minimizes the analysis error variance. Most of the time, information about the forecast and observational error is restricted to the knowledge of the first and second statistical moments that correspond to the mean and the error covariances, respectively. Used for several years in most meteorological centers, *optimal interpolation* seeks to apply this principle, but it does so only approximately. For instance, the forecast error covariances are not available, and they must be approximated as realistically as possible to render the problem tractable (Phillips 1986; Hollingsworth and Lönnberg 1986; Bartello and Mitchell 1992). Another difficulty with the operational practice of objective analysis is that data arriving at asynoptic times are not handled very well.

Sequential estimation refers to the continuous blending of data and model forecast as data come in. Within the context of a linear model, this can be done with the Kalman filter (Kalman 1960; Kalman and Bucy 1961), which is able to provide an optimal estimate minimizing the analysis error variance. Moreover, even though the Kalman filter is sequential, it provides the optimal solution at any time step, given the previous observations. Finally, the Kalman filter produces a forecast of both the model state and its error covariance. Therefore, information is given about the actual accuracy of the analysis, and this is what makes the Kalman filter unique. Some theoretical work has been done

---

* Permanent affiliation: Aerospace Meteorology Division/Atmospheric Environment Service, Dorval, Quebec, Canada.

Corresponding author address: Dr. Pierre Gauthier, ARMA/AES, 2121 Trans-Canada Highway, Dorval, Quebec, Canada H9P 1J3.

to extend this method to the nonlinear case, but one then faces the issue of the closure scheme for the different statistical moments that are needed to describe the error structure. One such method that relies on a low-order closure assumption is the so-called *extended Kalman filter* (EKF), which is used in this paper.

In the EKF framework, the time evolution of the forecast error is assumed to be accurately described by the tangent linear model (Lacarra and Talagrand 1988), obtained by linearizing the equations of the nonlinear model around a time-dependent solution or trajectory; this trajectory is obtained from an integration of the nonlinear model, using the current best estimate as initial conditions. The complex flow configuration that defines this linear model embeds instability processes that may lead to local error growth without any external forcing through model error. In the present paper, the focus is put on this particular kind of error growth, and no model error was therefore included. Identical-twin experiments have been carried out to stress the difference that exists between different data assimilation schemes (i.e., the EKF and an "improved" optimal interpolation) or between different datasets.

Since the analysis error variance is available, the Kalman filter and the EKF produce an analyzed state and give information about the state's accuracy. This makes it particularly well suited to study the impact of different datasets in the context of an observing system simulation experiment (OSSE). The first set of experiments presented in this paper is concerned with data simulated according to what is usually provided by the operational radiosonde network. In a second set of experiments, wind data from a proposed satellite-based Lidar instrument have been simulated and added to the radiosonde data. These experiments aimed at simulating data that will be produced by the Atmospheric Laser Doppler Instrument (ALADIN) of the European Space Agency and the Laser Atmospheric Wind Sounder (LAWS) of the National Aeronautics and Space Administration (NASA). Assimilation was carried out with the EKF for different satellite configurations to determine the one that would be the most beneficial for NWP.

In the next section, a short derivation of the equations of the EKF is presented, and the way it was implemented is discussed in section 3. Experiments with the radiosonde data are reported in section 4, while those including the lidar data are discussed in section 5. The paper ends with the conclusions in section 6. Two appendixes are also included to give some details about the "adjoint interpolation" (appendix A) and about the method used to initialize the forecast error covariances in spectral space (appendix B).

2. The extended Kalman filter

The derivation of the filter equations presented here follows that given in Ghil (1989) for the linear case. If $\mathbf{X} \in R^n$ stands for the model state of the dynamical system

$$\frac{d\mathbf{X}}{dt} = \mathbf{f}(\mathbf{X}), \tag{2.1}$$

its integration from time t_{k-1} up to t_k, using $\mathbf{X}_{k-1}$ as initial conditions, can be represented symbolically by the relation

$$\mathbf{X}_k = \mathcal{F}_{k-1}(\mathbf{X}_{k-1}). \tag{2.2}$$

The analysis cycle then proceeds by using a forecast as a first guess, which is corrected in order to better fit the data available at time t_k. The analysis $\mathbf{X}_k^a$ at time t_k is then given by

$$\begin{aligned} \mathbf{X}_k^f &= \mathcal{F}_{k-1}(\mathbf{X}_{k-1}^a), \\ \mathbf{X}_k^a &= \mathbf{X}_k^f + \mathbf{K}_k[\mathbf{Z} - \mathbf{H}_k(\mathbf{X}_k^f)], \end{aligned} \tag{2.3}$$

where the nonlinear operator $\mathbf{H}_k$ stands for the *generalized interpolation* (or *forward interpolation*) of the model state to the observations, $\mathbf{Z}_k$ are the observed quantities, and $\mathbf{K}_k$ is the *gain matrix.* As in optimal interpolation, the gain matrix $\mathbf{K}_k$ appearing in (2.3) is determined by minimizing a quadratic measure of the analysis error

$$J = \mathcal{E}(\mathbf{X}_k^a - \mathbf{X}_k^t)^{\mathrm{T}}\mathbf{A}(\mathbf{X}_k^a - \mathbf{X}_k^t),$$

where $\mathbf{A}$ is any arbitrary positive semidefinite matrix, $\mathcal{E}$ stands for the statistical expectancy, and the optimal weights depend on the forecast error covariance, which must be known. By taking $\mathbf{A}$ to be identically zero with the exception of one element of its diagonal, it is seen that this minimizes the error variance for each component of the model state vector. It should also be pointed out that the minimum variance criterion is just one of the different ways of deriving the Kalman filter (see Ghil et al. 1981; Jazwinski 1970).

As discussed in Jazwinski (1970), the extension to the nonlinear case can be achieved in many ways, one of which is the extended Kalman filter. It is based on the assumption that the forecast error $\delta\mathbf{X}$ resulting from a change $\delta\mathbf{X}_0$ to the initial conditions can be well approximated by a linear model referred to as the *tangent linear model* (Le Dimet and Talagrand 1986). If $\mathbf{X}_s(t)$ is the *trajectory* obtained by integrating the nonlinear model with the initial conditions $\mathbf{X}_0$, the tangent linear model stems from the linearization of (2.1) around this trajectory and can be symbolically expressed as

$$\frac{d}{dt}\delta\mathbf{X} = \frac{\partial\mathbf{f}}{\partial\mathbf{x}}[\mathbf{X}_s(t)]\delta\mathbf{X}, \tag{2.4}$$

$\partial\mathbf{f}/\partial\mathbf{x}$ being the Jacobian of $\mathbf{f}(\mathbf{X})$. The validity of this approximation has been tested by Lacarra and Talagrand (1988) and Vukicewic (1991) by comparing results obtained for $\delta\mathbf{X}$ by using either (2.4) or the nonlinear model. In both of these studies, the tangent linear model was shown to give an accurate estimate of the error for time periods of 24 h that correspond to those considered in this paper. The validity of the tangent linear assumption in the presence of baroclinic instability has also been studied in detail in Rabier and Courtier (1992).

The forecast model being imperfect, the true atmospheric state ($\mathbf{X}^t$) at time t_k is given by

$$\mathbf{X}_k^t = \mathcal{F}_{k-1}(\mathbf{X}_{k-1}^t) + \mathbf{b}_{k-1}^q, \qquad (2.5)$$

where the model error, $\mathbf{b}_{k-1}^q$, is deemed to be unbiased and uncorrelated in time. In other words,

$$\mathcal{E}\mathbf{b}_k^q = 0, \quad \mathcal{E}\mathbf{b}_k^q(\mathbf{b}_l^q)^{\mathrm{T}} = \mathbf{Q}_k\delta_{k,l}, \qquad (2.6)$$

where the superscript T stands for the matrix transpose while the matrix $\mathbf{Q}_k$ contains all the information about the model error covariance. In a similar way, the observational error (including instrument and representativeness error) $\mathbf{b}_k^0$ is such that

$$\mathbf{Z}_k = \mathbf{H}_k(\mathbf{X}_k^t) + \mathbf{b}_k^0, \qquad (2.7)$$

and

$$\mathcal{E}\mathbf{b}_k^0 = 0, \quad \mathcal{E}\mathbf{b}_k^0(\mathbf{b}_l^0)^{\mathrm{T}} = \mathbf{R}_k\delta_{k,l}. \qquad (2.8)$$

The covariance matrix $\mathbf{R}_k$ models not only the measurement error but also error associated with the forward interpolation. Finally, observation and forecast errors are assumed to be uncorrelated at all times, thereby implying that for all k and l

$$\mathcal{E}\mathbf{b}_k^q(\mathbf{b}_l^0)^{\mathrm{T}} = 0. \qquad (2.9)$$

The forecast ($\mathbf{P}_k^f$) and analysis ($\mathbf{P}_k^a$) error covariances are defined as

$$\mathbf{P}_k^f = \mathcal{E}(\mathbf{X}_k^f - \mathbf{X}_k^t)(\mathbf{X}_k^f - \mathbf{X}_k^t)^{\mathrm{T}},$$

$$\mathbf{P}_k^a = \mathcal{E}(\mathbf{X}_k^a - \mathbf{X}_k^t)(\mathbf{X}_k^a - \mathbf{X}_k^t)^{\mathrm{T}},$$

and the forecast error is obtained from

$$\mathbf{X}_k^f - \mathbf{X}_k^t = [\mathcal{F}_{k-1}(\mathbf{X}_{k-1}^a) - \mathcal{F}_{k-1}(\mathbf{X}_{k-1}^t)] - \mathbf{b}_{k-1}^q.$$

Using the tangent linear model to approximate the term between brackets, one obtains

$$\mathbf{X}_k^f - \mathbf{X}_k^t \approx \mathcal{A}_{k-1}(\mathbf{X}_{k-1}^a - \mathbf{X}_{k-1}^t) - \mathbf{b}_{k-1}^q,$$

where the linear operator $\mathcal{A}_{k-1}$ stands for the integration of the tangent linear model from time t_{k-1} up to time t_k; the tangent linear model is obtained by linearizing around the trajectory obtained by using the current best estimate of the model state $\mathbf{X}_{k-1}^a$ as initial conditions. The forecast error covariance is then shown to be

$$\mathbf{P}_k^f = \mathcal{A}_{k-1}\mathbf{P}_{k-1}^a\mathcal{A}_{k-1}^{\mathrm{T}} + \mathbf{Q}_{k-1}. \qquad (2.10)$$

The tangent linear approximation is also applied to the interpolation operator, in which case

$$\mathbf{H}_k(\mathbf{X}_k^f) - \mathbf{H}_k(\mathbf{X}_k^t) \approx \mathbf{H}_k'(\mathbf{X}_k^f - \mathbf{X}_k^t),$$

with $\mathbf{H}_k' \equiv \partial\mathbf{H}_k/\partial\mathbf{X}_k$ representing the linearization of $\mathbf{H}_k$ around the model state $\mathbf{X}_k^f$. This allows the analysis error covariance to be written as

$$\mathbf{P}_k^a = (\mathbf{I} - \mathbf{K}_k\mathbf{H}_k')\mathbf{P}_k^f(\mathbf{I} - \mathbf{H}_k'^{\mathrm{T}}\mathbf{K}_k^{\mathrm{T}}) + \mathbf{K}_k\mathbf{R}_k\mathbf{K}_k^{\mathrm{T}}. \qquad (2.11)$$

As mentioned earlier, the optimal gain matrix $\mathbf{K}_k$ is obtained by minimizing the analysis error variance and is shown to be (cf. Ghil 1989)

$$\mathbf{K}_k^* = \mathbf{P}_k^f\mathbf{H}_k'^{\mathrm{T}}(\mathbf{R}_k + \mathbf{H}_k'\mathbf{P}_k^f\mathbf{H}_k'^{\mathrm{T}})^{-1}, \qquad (2.12)$$

which, when substituted in (2.11), yields that

$$\mathbf{P}_k^a = (\mathbf{I} - \mathbf{K}_k\mathbf{H}_k)\mathbf{P}_k^f \qquad (2.13)$$

at optimality.

The EKF equations correspond to (2.3), (2.10), (2.12), and (2.13), and their integration requires initial conditions for the first-guess $\mathbf{X}_0^f$ and its error covariance $\mathbf{P}_0^f$. The assimilation is assumed to start with the analysis cycle and then to proceed with the integration of the resulting analyzed model state and analysis error covariance. The EKF equations are then summarized as follows:

$$\begin{aligned}
&(\mathrm{a})\ \mathbf{K}_{k-1} = \mathbf{P}_{k-1}^f\mathbf{H}_{k-1}'^{\mathrm{T}}(\mathbf{R}_{k-1} + \mathbf{H}_{k-1}'\mathbf{P}_{k-1}^f\mathbf{H}_{k-1}'^{\mathrm{T}})^{-1},\\
&(\mathrm{b})\ \mathbf{X}_{k-1}^a = \mathbf{X}_{k-1}^f + \mathbf{K}_{k-1}[\mathbf{Z}_{k-1} - \mathbf{H}_{k-1}(\mathbf{X}_{k-1}^f)],\\
&(\mathrm{c})\ \mathbf{P}_{k-1}^a = (\mathbf{I} - \mathbf{K}_{k-1}\mathbf{H}_{k-1}')\mathbf{P}_{k-1}^f\\
&(\mathrm{d})\ \mathbf{X}_k^f = \mathcal{F}_{k-1}(\mathbf{X}_{k-1}^a)\\
&(\mathrm{e})\ \mathbf{P}_k^f = \mathcal{A}_{k-1}\mathbf{P}_{k-1}^a\mathcal{A}_{k-1}^{\mathrm{T}} + \mathbf{Q}_{k-1}, \qquad (2.14)
\end{aligned}$$

where the * notation for the optimal weights is now implicit.

The *observational error covariance* $\mathbf{R}_k$ must be specified; it depends on the type of observation and is related to the measurement and forward interpolation errors but also to the natural variability of the atmospheric flow on scales that are not resolved by the assimilating model. The knowledge of the model error $\mathbf{Q}_k$ is also required, and its determination could be done adaptively (Bélanger 1974; Dee et al. 1985) by making the *innovation vector* sequence $[\mathbf{Z}_k - \mathbf{H}_k(\mathbf{X}_k^f)]$ uncorrelated in time. This is a very costly proposition and in most studies (e.g., Cohn and Parrish 1991; Dee 1991) the model error covariance is specified and the form used has to be justified. The model error can be associated with the discretization error or the absence of some dynamical processes in the numerical model (e.g., imperfect parameterization of the subgrid-scale processes). The work of Phillips (1986) investigates the validity of such approximations, and a discussion of this question in relation to the Kalman filter is presented in Cohn and Parrish (1991). It is important to keep in mind that the results may depend crucially on what is used for the model and observational error (Daley 1992).

In the limit where the nonlinearities become negligible, the EKF is optimal and corresponds to the usual Kalman filter. In the nonlinear case, its optimality could be verified through a Monte Carlo simulation out of which the forecast covariances can be estimated and compared to what the EKF produces. This is directly related to the validity of the tangent linear approximation that, as discussed above, has been shown to be a reasonably good one for barotropic models over a 24-h time interval.

By providing the analysis error variance, the EKF is able to supply a measure of the accuracy of an analysis, and therefore it allows the impact of different observation sets to be compared. By using simulated observations, this can be used to look at different configurations for a proposed satellite instrument or network of observing stations to find the one that can be expected to be the most beneficial from the point of view of numerical prediction. A study of this type has been carried out recently by Cohn and Parrish (1991), who looked at the impact of wind profiler data on the analysis and forecast error by employing a linear Kalman filter.

In the present study, an EKF based on the barotropic vorticity equation will be used. Although linear, the model used by the EKF to integrate the forecast error has variable coefficients (in space and time), and its dynamic is substantially more complex than a linear model with constant coefficients such as the one used by Cohn and Parrish (1991). In the next section, the implementation of the EKF is described.

3. Implementation of the extended Kalman filter

The EKF has been implemented within the framework of the Action de Recherche Petite Echelle Grande Echelle (ARPEGE) Integrated Forecasting System (IFS) model currently being developed by the European Centre for Medium-Range Forecasts (ECMWF) and Météo-France; this project's characteristics are described in Thépaut and Courtier (1991). Since the term "model" usually refers to the temporal integration and the way it is done (i.e., numerical and parameterization schemes employed, nature of the boundary conditions, etc.), it is more appropriate to think of ARPEGE IFS as a programming environment because it provides the means to do many different types of applications such as 3D and 4D variational assimilation, predictability studies, assimilation with an EKF, search for most unstable modes, etc. At heart, ARPEGE IFS is a spectral global model with variable resolution (Courtier and Geleyn 1988), and it can be run in different configurations (barotropic vorticity equation, barotropic shallow-water equations, or primitive equations). The present paper will be concerned only with the specifics of the implementation of the EKF in the particular context of the barotropic vorticity equation

$$\frac{\partial \zeta}{\partial t} + J(\psi, \zeta + f) = 0,$$

where ψ, ζ, and f are the streamfunction, the relative vorticity, and the planetary vorticity, respectively, while $J(a, b)$ stands for the Jacobian operator. Within the ARPEGE IFS environment, there are actually three models available for any configuration: the *direct model* (2.1), the *tangent linear model* (2.4), and the *adjoint model*. For a detailed discussion of the derivation of the adjoint model, the reader is referred to Talagrand and Courtier (1987) for the case of the barotropic vorticity equation, Courtier and Talagrand (1991) for the shallow-water case, and Thépaut and Courtier (1992) for the adiabatic primitive equations; all of these cases have already been discussed in Courtier (1987).

When implementing the EKF in this environment, it is important to notice that the linear operators $\mathcal{A}_{k-1}$ and $\mathbf{H}'_{k-1}$ appearing in (2.14) are not explicitly known as matrices; they are known only through their action on some vector $\mathbf{X}$. The tangent linear model being available, the calculation of

$$\mathbf{M}_k = \mathcal{A}_{k-1}\mathbf{P}^a_{k-1}$$

is done by performing N integrations of the tangent linear model from t_{k-1} up to t_k using successively the N columns of $\mathbf{P}^a_{k-1}$ as initial conditions and replacing the corresponding column with the result; proceeding in this way, only one $N \times N$ matrix is required. Finally, one gets that

$$\mathbf{P}^f_k = \mathcal{A}_{k-1}\mathbf{P}^a_{k-1}\mathcal{A}^{\mathrm{T}}_{k-1} = (\mathcal{A}_{k-1}\mathbf{M}^{\mathrm{T}}_k),$$

and this requires N more integrations of the tangent linear model now using the rows of $\mathbf{M}_k$ as initial conditions. The cost of integrating the forecast error covariances therefore corresponds to that of $2N$ integrations of the tangent linear model. For a barotropic vorticity equation model truncated at T21, a 24-h integration of the EKF with a 1-h time step was done in 1100 s of CPU time on a CRAY 2 computer, and this is certainly not out of reach.

The linearized forward interpolation operator $\mathbf{H}'_{k-1}$ is also not known explicitly as a matrix, but if it was, (2.14a)–(2.14c) could be solved with matrix operations involving only one ($M \times M$) matrix inversion, M being the number of observations. In the operational practice, M can be large and this operation can be time consuming. A simplification to the implementation can be achieved by a serial processing of observations where observations having correlated errors are collected together, thereby forming "p" groups of "m_p" observations; the observation errors are uncorrelated between each group, and $\mathbf{R}_k$ is then block diagonal. In that case, if $\mathbf{H}_k$ is linear, the sequentiality of the Kalman filter can be used to show that the analysis cycle can be solved iteratively (see Jazwinski 1970; Brown 1983). Setting $\mathbf{P}^{(0)}_{k-1} = \mathbf{P}^f_{k-1}$ and $\mathbf{X}^{(0)}_{k-1} = \mathbf{X}^f_{k-1}$, for $l = 1, \cdots, p$, the equations

$$\begin{aligned}
&(\mathrm{a})\ \mathbf{K}^{(l)}_{k-1} = \mathbf{P}^{(l-1)}_{k-1}\mathbf{H}^{(l)\mathrm{T}}_{k-1}[\mathbf{R}^{(l)}_{k-1} + \mathbf{H}^{(l)}_{k-1}\mathbf{P}^{(l-1)}_{k-1}\mathbf{H}^{(l)\mathrm{T}}_{k-1}]^{-1},\\
&(\mathrm{b})\ \mathbf{X}^{(l)}_{k-1} = \mathbf{X}^{(l-1)}_{k-1} + \mathbf{K}^{(l)}_{k-1}[\mathbf{Z}_l - \mathbf{H}^{(l)}_{k-1}\mathbf{X}^{(l-1)}_{k-1}],\\
&(\mathrm{c})\ \mathbf{P}^{(l)}_{k-1} = [\mathbf{I} - \mathbf{K}^{(l)}_{k-1}\mathbf{H}^{(l)}_{k-1}]\mathbf{P}^{(l-1)}_{k-1} \qquad (3.1)
\end{aligned}$$

are solved iteratively to obtain that $\mathbf{P}^a_{k-1} = \mathbf{P}^{(p)}_{k-1}$ and $\mathbf{X}^a_{k-1} = \mathbf{X}^{(p)}_{k-1}$. In particular, if the observational errors are assumed to be uncorrelated, the result should be independent of the way the observations are regrouped; (3.1) could be solved by treating all observations one by one or as a whole without changing the result. This property provides a very powerful test of the computer code used for the forward interpolation. This treatment also requires a lot less memory to store $\mathbf{H}_k$ and $\mathbf{K}_k$.

The forward interpolation $\mathbf{H}_k$ summarizes all operations needed to go from the model state $\mathbf{X}_k$ to the observations. For a model based on the barotropic vorticity equation, $\mathbf{X}$ is defined by the spectral components $\tilde{\zeta}$ of the vorticity. For an observation of a single wind component along a given direction, the associated forward interpolation is linear and corresponds to the following sequence of operations:

(i) solve spectrally the Poisson equation $\nabla^2\psi = \zeta$ to obtain the spectral components of the streamfunction ψ (defined as operator $\mathcal{P}$);

(ii) calculate the spectral wind components $\tilde{u}$ and $\tilde{v}$ (defined as operator $\mathcal{U}$);

(iii) perform an inverse spectral transform to get the two wind components on the Gaussian grid (defined as operator $\mathcal{S}^{-1}$);

(iv) interpolate bilinearly both wind components to the observation point (defined as operator $\mathcal{B}$);

(v) project the model wind in the direction along which the measurement is taken (defined as operator Π).

This is what would be needed for the direct assimilation of Doppler wind data such as those obtained either from a radar or a lidar instrument. The operator $\mathbf{H}'_k$ can be written as

$$\mathbf{H}'_k = \Pi\mathcal{B}\mathcal{S}^{-1}\mathcal{U}\mathcal{P}. \qquad (3.2)$$

The first three operators (i.e., $\mathcal{P}$, $\mathcal{U}$, and $\mathcal{S}^{-1}$) involve only one spectral transform and can be done once to obtain a model state on the Gaussian grid. However, the EKF equations involve products such as $\mathbf{H}'_k\mathbf{P}^f_k$, and this calls for N spectral transforms. A close look at (2.13) shows that $4N$ spectral transforms are needed, while, on the other hand, $\mathbf{H}'_k$ can be explicitly built with N spectral transforms by forward interpolating the N columns of the $(N \times N)$ identity matrix. The matrix $\mathbf{H}'_k$ must be stored, but this does not require too much memory if (3.1) is used.[1]

The assimilation of geopotential observations requires this variable to be related to the model state through the nonlinear balance equation

$$\Delta\phi = \nabla\cdot[(\zeta + f)\nabla\Delta^{-1}\zeta] - \frac{1}{2}\nabla\Delta^{-1}\zeta\cdot\nabla\Delta^{-1}\zeta, \qquad (3.3)$$

where Δ stands for the Laplacian operator. At midlatitudes, the planetary vorticity f being usually more important than the relative vorticity ζ, (3.3) can be approximated by linearizing around a state of rest to give the linear balance equation

$$\phi' = \Delta^{-1}[\nabla\cdot(f\nabla\Delta^{-1}\zeta)] \equiv \mathcal{L}_0\zeta'. \qquad (3.4)$$

However, situations may occur where strong wind shears exist, leading to an important local vorticity, in which case ζ may not be negligible with respect to f: this is also the case in the equatorial region. It could then be more appropriate to linearize (3.3) around a reference state ζ_s:

$$\phi' = \Delta^{-1}\{\nabla\cdot[(\zeta_s + f)\nabla\Delta^{-1}\zeta'] + \nabla\cdot(\zeta'\nabla\Delta^{-1}\zeta_s) - \nabla\Delta^{-1}\zeta'\cdot\nabla\Delta^{-1}\zeta_s\} \equiv \mathcal{L}_{\mathcal{S}}\zeta'. \qquad (3.5)$$

For sake of simplicity, the linear balance equation (3.4) will be used in this paper, and therefore, $\mathbf{H}_k$ is linear and

$$\mathbf{H}_k = \mathbf{H}'_k = \mathcal{B}\mathcal{S}^{-1}\mathcal{L}_0.$$

The validation of the computer code was made by performing an identical-twin experiment based on the barotropic vorticity equation spectrally truncated at T21. The observations were simulated by integrating the model with initial conditions $\mathbf{X}^t_0$ and then forward interpolating the model state to a given set of points for an observation of u, v, or ϕ. If the assimilation uses $\mathbf{X}^t_0$ as the first guess, (2.14) shows that the innovation vector should always identically vanish, and therefore, $\mathbf{X}^a_k = \mathbf{X}^f_k$ for all k. This test verifies that $\mathbf{H}_k$ is correct, but the analysis cycle can be tested even more by noticing that for uncorrelated observational errors $\mathbf{R}_k$ is diagonal and, $\mathbf{H}_k$ being linear, (3.1) applies, and the result of the analysis should be independent of the sizes of the p observation packets. By making the analysis with different packet sizes, the same results should be obtained for $\mathbf{X}^a_k$ and $\mathbf{P}^a_k$. These tests were performed for every type of observation used to ensure that there were no errors in the analysis part of the EKF. Finally, the validity of (2.14) is related to that of the tangent linear model that had been previously tested for the implementation of the adjoint model (Thépaut and Courtier 1991).

In the experiments to be described in the following sections, $\mathbf{P}^f_0$ was initialized by assuming the first-guess error correlation on the streamfunction to be homogeneous and isotropic. This point is discussed at length in appendix B, where it is also shown that under these conditions $\mathbf{P}^f_0$ is diagonal. This representation is the basis of the implementation of the 3D variational assimilation system of Derber et al. (1991) [described in detail in Parrish and Derber (1992)] and also of the formulation used in ARPEGE IFS (Pailleux 1990). The aim here was to choose something reasonable, although the correct form can be obtained by integrating the EKF over a sufficiently long time so that the forecast error covariance converges to the asymptotic form that

---

[1] It is shown in appendix A that the adjoint interpolation can be used to obtain $\mathbf{H}'_k$ with only m_p spectral transforms; this is useful when the number of observations is less than the number of model variables.

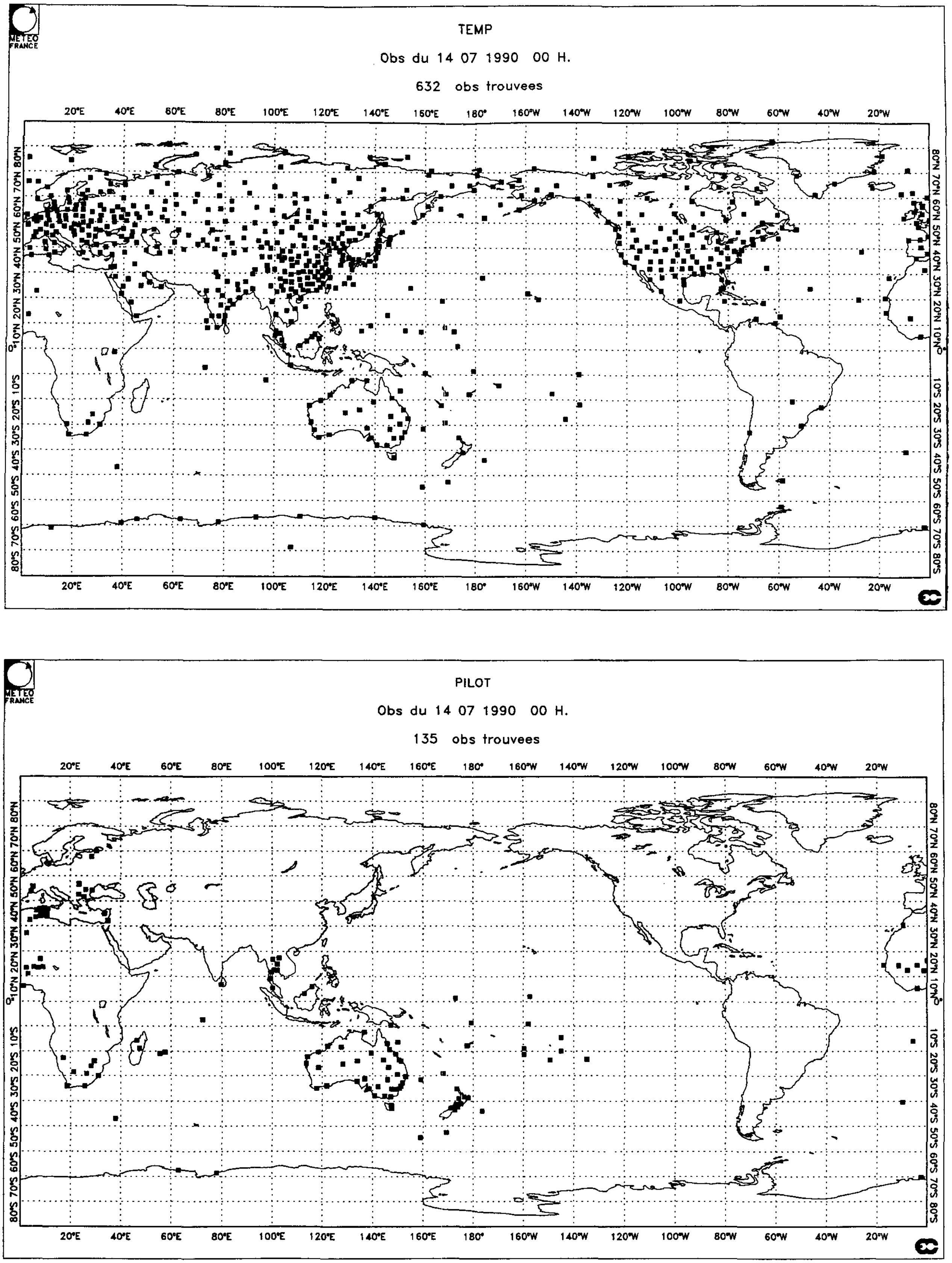

FIG. 1. Typical radiosonde network at 0000 UTC for TEMP and PILOT. This network is assumed to be the same every 6 h.

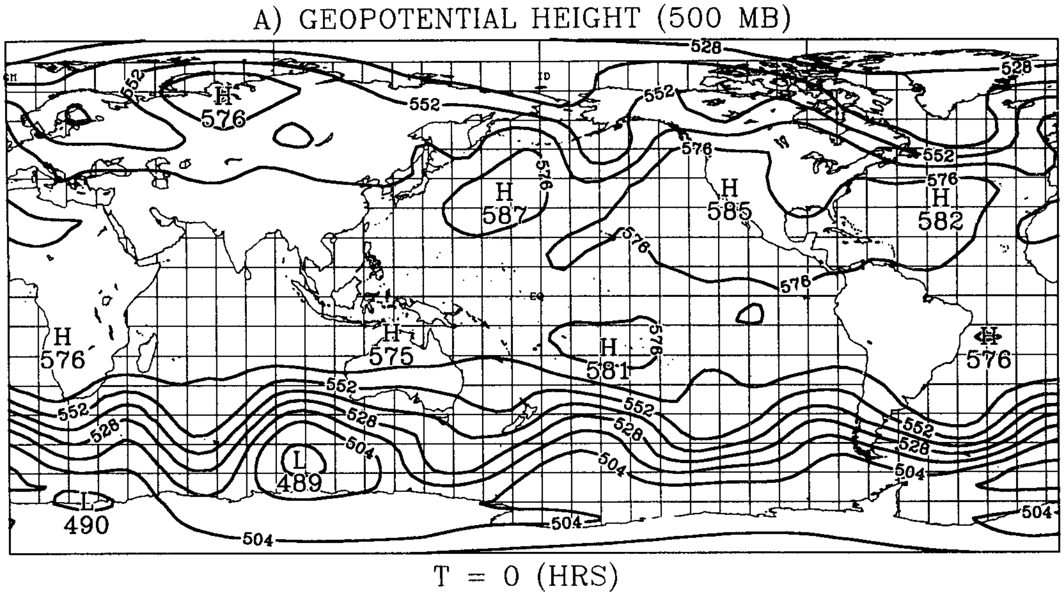

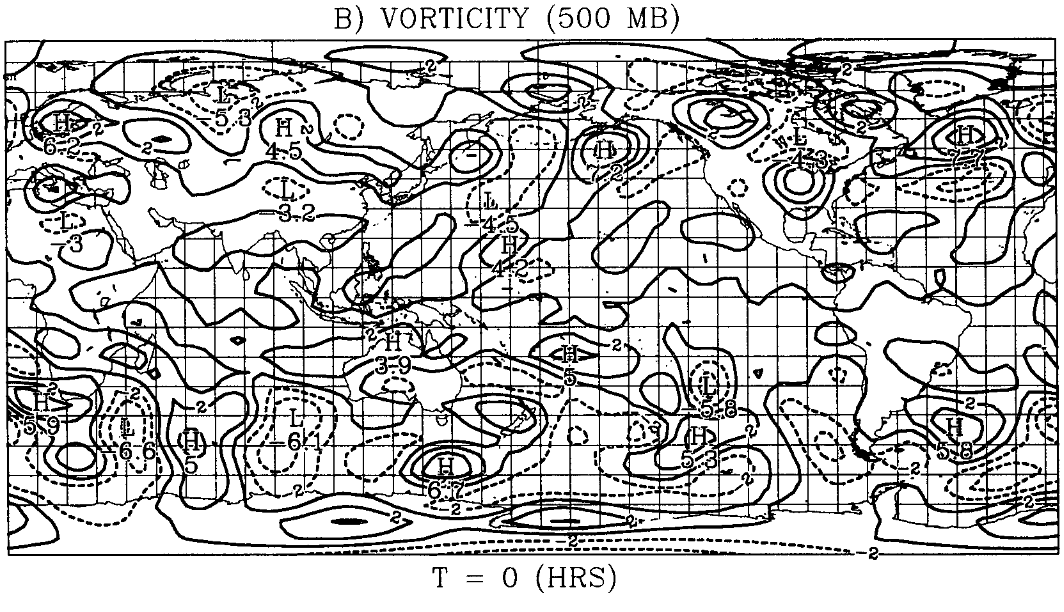

FIG. 2. Initial conditions on 14 July 1990: (a) geopotential field and (b) vorticity field.

it would reach for a stationary observation network (Daley 1991). In that respect, a study of the impact of the initial choice for $\mathbf{P}_0^f$ on the results is certainly of interest.

The error covariance of the model state corresponds to the spectral components of the vorticity, but the wind or geopotential error covariances at grid points can easily be obtained from it. For instance, the zonal-wind error $\mathbf{u}'$ on the Gaussian grid is linked to the spectral vorticity error through the relation

$$\mathbf{u}' = \mathcal{S}^{-1}\Pi_u \mathcal{U}\mathcal{P}\tilde{\zeta}' \equiv G_u\tilde{\zeta}',$$

with Π_u representing the projection of the model wind in the zonal direction and the vector $\mathbf{u}'$ referring to the gridpoint values of the zonal-wind error. It then follows that the zonal-wind error covariance $\mathbf{P}_{uu}$ (analysis or forecast) is

$$\mathbf{P}_{uu}^{f,a} = \mathbf{G}_u \mathbf{P}_k^{f,a} \mathbf{G}_u^{\mathrm{T}}.$$

The same can be done for the meridional wind component to obtain that

$$\mathbf{P}_{vv}^{f,a} = \mathbf{G}_v \mathbf{P}_k^{f,a} \mathbf{G}_v^{\mathrm{T}}.$$

-A-

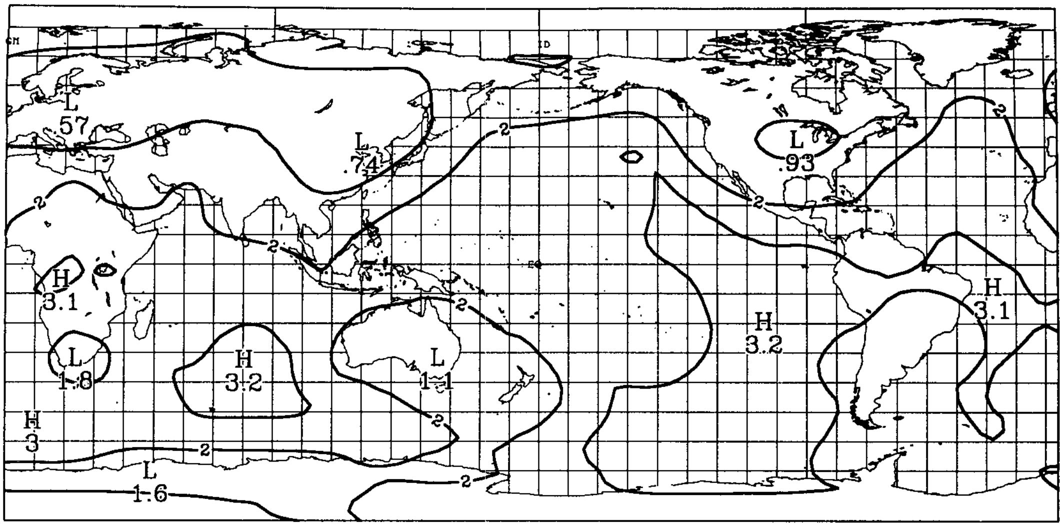

T = 0 (HRS)

-B-

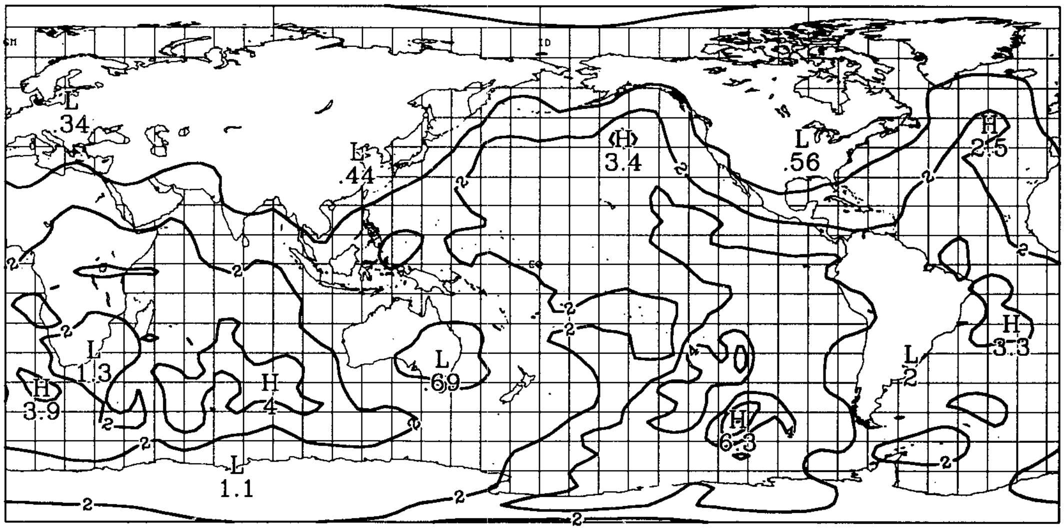

T = 12 (HRS)

FIG. 3. Analysis error variance resulting from an assimilation with the extended Kalman filter: (a) $t = 0$ h, (b) 12 h, and (c) 24 h. Units used are 1×10^{-12} s^{-2}, with contour levels of 1 unit, and the characteristic length of the first-guess error is 1200 km.

Finally, the error on the geopotential being

$$\phi' = \mathcal{B}\mathcal{S}^{-1}\mathcal{L}_0\tilde{\zeta}' \equiv G_\phi\tilde{\zeta}',$$

the geopotential error covariance is

$$\mathbf{P}^{f,a}_{\phi\phi} = \mathbf{G}_\phi\mathbf{P}^{f,a}_{k}\mathbf{G}^{\mathrm{T}}_{\phi}.$$

These relations also allow the wind and geopotential error correlations to be computed. In the next section, results obtained with the EKF are presented.

4. Experiments with a simulated radiosonde network

All experiments in this paper use synthetic data and are of the identical-twin type (Daley 1991). Consequently, no model error is taken into account, and as pointed out in Cohn and Parrish (1991), this can imply that there is no global error growth, but as will be seen shortly, this is not the case. Another consequence of having no model error is that it usually produces results

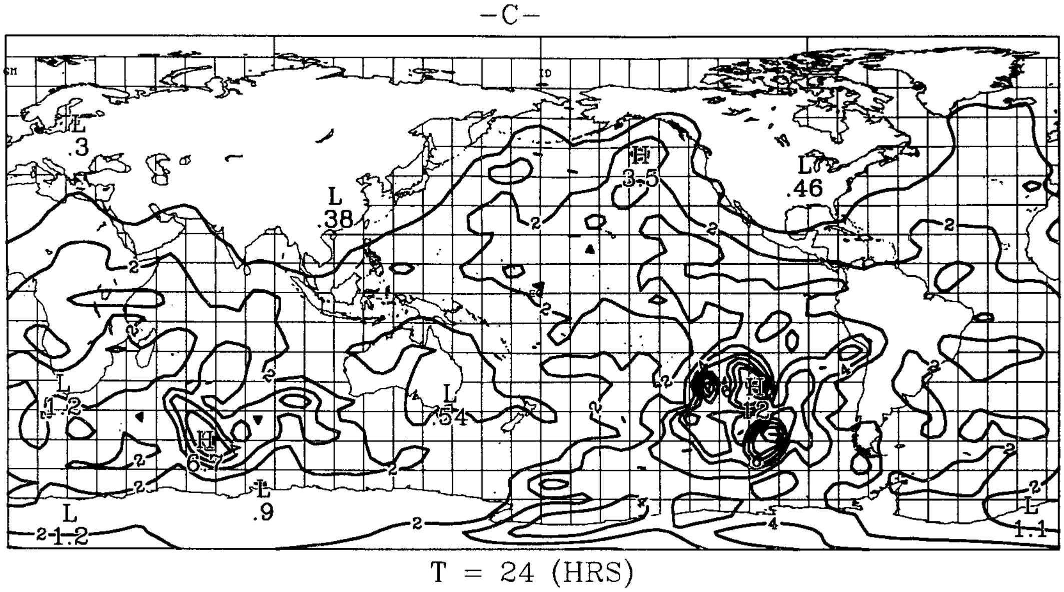

FIG. 3. (*Continued*)

that are too optimistic. The observations have been simulated according to the radiosonde network for measurements of wind and geopotential at 500 mb associated with the 633 TEMP stations, and wind only for the 135 PILOT stations; all reporting stations at 0000 UTC 14 July 1990 have been considered. As can be seen from Fig. 1, this observation network covers the continents of the Northern Hemisphere rather well but gives only a weak coverage of the oceanic regions, with important data voids especially in the Southern Hemisphere. Synthetic observations were generated from a 24-h integration of the barotropic vorticity equation spectrally truncated at T21, the initial conditions $\mathbf{X}_0^t$ used were those of 0000 UTC 14 July 1990, and the associated geopotential height and vorticity fields are shown in Fig. 2. At the location of each station, values of u, v, and ϕ have been generated every 6 h for 24 h according to what would be provided by the station; the network has been assumed to be the same for each synoptic time. In reality, the radiosonde network has a periodicity of 12 h, not 6 h, but the choice made here can be justified by the fact that various other sources of information such as the new automated aircraft data, have not been considered here. The forward interpolation for ϕ was taken to be linear and to correspond to $\mathcal{L}_0$ as described in the previous section. No noise was added to the interpolated model state, but observational error is introduced at the assimilation stage; it has been assumed to be uncorrelated with standard deviations of 2.24 m s^{-1} and 11.2 m on wind and geopotential height observations; these are operational estimates of the error made by radiosondes.

Assimilation with the EKF was then accomplished in the following way. The first-guess error covariance $\mathbf{P}_0^f$ has been initialized as explained in appendix B; the correlation length of the correlation function was set to 1200 km, while the uniform variance corresponds to that of a geopotential error level of 21 m (standard deviation) at midlatitudes. The focus will not be on the analysis itself but on the time evolution of the covariances that can be influenced by the nature and distribution of observations (through the interpolation $\mathbf{H}'_k$), their error structure (through $\mathbf{R}_k$), and the initial assumptions made on $\mathbf{P}_0^f$. Moreover, the first guess is taken to correspond to $\mathbf{X}_0^t$, thereby implying that $\mathbf{X}_k^a = \mathbf{X}_k^f$ at all times because the observations correspond to an exact model state. By proceeding in this manner, only (2.14a), (2.14c), and (2.14e) are active in the EKF equations, (2.14d) being needed only to define the tangent linear model that is therefore a linearization around the true trajectory.

By choosing the initial estimate of $\mathbf{P}_0^f$ to correspond to what is found for the operational analysis error level, the time evolution of the forecast error covariance should not be very different from what would be obtained by linearizing around the current best estimate instead of the true solution because the tangent linear model has been verified to give an accurate representation of the forecast error over a 24-h time interval (Courtier and Talagrand 1987; Lacarra and Talagrand 1988); this holds for the large scales resolved by the T21 barotropic model used here. This would cease to be true, however, if the assimilation was made over periods of time that exceed the limit of validity of the tangent linear model. As a result, the assimilation deviates from a strict implementation of the extended Kalman filter, but the time evolution of the forecast error covariance should not be significantly different.

Figure 3 shows the analysis error variance at $t = 0$, 12, and 24 h. At $t = 0$, it is as it would be if optimal interpolation was used, but when the time dimension comes into play, the variance is now governed by the tangent linear model that captures the dynamics of error growth and propagation of information. This is clearly illustrated by Figs. 3b,c, showing that the region west of South America experiences a significant increase in the error level that can be attributed to three factors. First of all, a more important error growth rate is hinted at by the local vorticity gradient that points toward local barotropic instability in the area: this can be seen in Fig. 4a, where the vorticity and the error variance over that region have been plotted at the end of the assimilation time interval. The maximum variance in that area is about four times the initial constant level, and the error has therefore doubled in 24 h. Second, this area being totally devoid of any observations, nothing acts to bring the error level down. Finally, the geopotential (shown in Fig. 4b) indicates that the circulation tends to skirt the area and propagation of information from the outside is therefore impaired.

A) ERROR VARIANCE AND VORTICITY

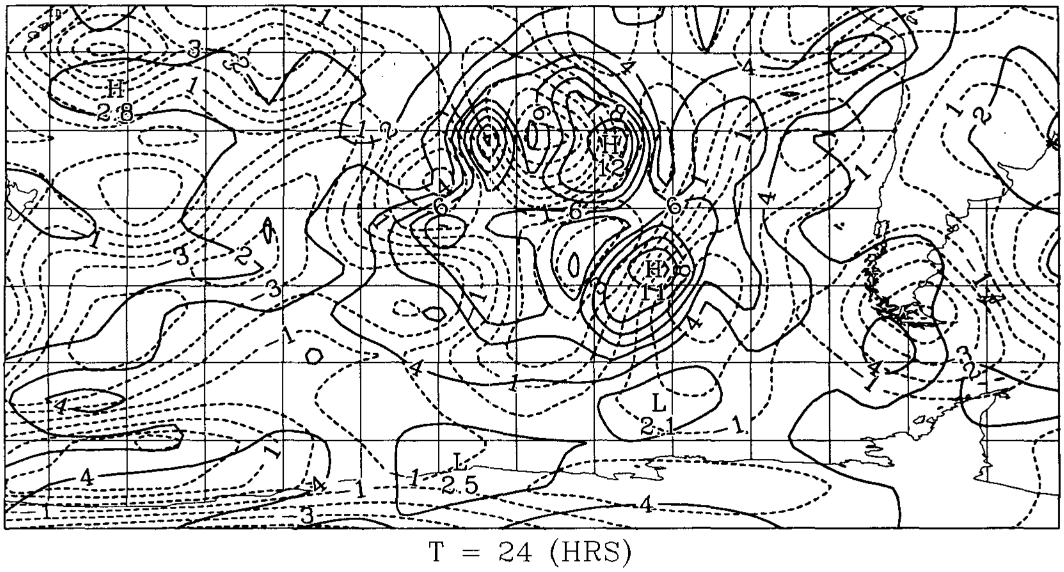

B) ERROR VARIANCE AND GEOPOTENTIAL

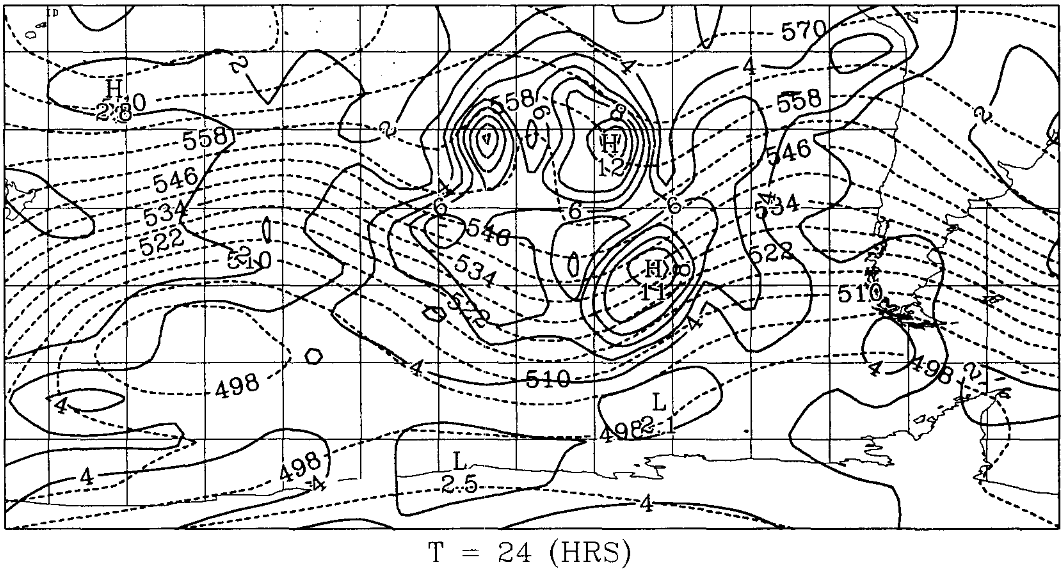

FIG. 4. Analysis error variance field at t = 24 h superposed over (a) the vorticity field and (b) the geopotential field. The domain is a close-up of the region west of South America.

Without the time integration of the forecast error covariances, one has only to solve (2.14a) and (2.14c) to update the analysis error covariances according to information brought in by new observations. Proceeding in this way is an improvement over optimal interpolation in that the analysis error covariance is updated and that no data selection algorithm is involved. The resulting analysis is represented at the final time in Fig. 5. A comparison with the variance field of Fig. 3c obtained with the EKF shows that this "improved" optimal interpolation is not giving a good estimate of the accuracy of the analysis. The conclusion is then that the EKF brings important and new information about the actual accuracy of the analysis, which is seen to be quite different from the picture obtained from optimal interpolation that uses an incorrect estimate of the forecast error covariance. The reason for this is that the EKF takes into account the dynamics of error growth and propagation of information by integrating in time the forecast error with the tangent linear model. The latter being obtained from a linearization of the model's equations around a complex time-dependent flow configuation, its dynamics embeds instability processes; this leads to error growth (even in the absence of model error) that depends on the local flow configuration. Propagation of information is also more accurate, and the presence of areas of closed circulations would tend to block information from entering in those regions. These mechanisms are seen to be quite different from those in an operational data assimilation cycle, where error growth is taken into account usually by increasing the uniform error variance linearly in time, which increases it globally regardless of the particularities due to local instabilities, lack of observations, etc.

The results may also depend on what is used to initialize the forecast error covariance. For instance, the correlation length used in the experiments reported above was 1200 km, which means that observations had an impact over a very large region. To assess the impact of this particular choice, the experiment was repeated using 400 km as the characteristic scale of the initial first-guess forecast errors; the resulting error variance fields are presented on Fig. 6. As can be seen from Fig. 6, the results show that the error level is considerably higher even at the initial time. This is a direct consequence of the reduced characteristic scale; by keeping the geopotential error field (and, hence, the streamfunction) to be the same as in the previous experiments (21 m), the corresponding vorticity error is increased since it is obtained by differentiating the streamfunction twice, and this makes the characteristic scale appear at the denominator. However, the general features of the variance field are very similar to those reported earlier (Fig. 3); in particular, the regions of intense error growth are still present. Finally, for the two cases discussed earlier, Fig. 7 shows the time evolution of the analysis error variance averaged over the globe for these two cases; to emphasize the impact of having a denser observation network, the contributions to the global mean coming from the Northern and Southern hemispheres have also been plotted. This clearly shows the analysis to be poorer in the Southern Hemisphere in both cases and the global reduction in analysis error to be done mostly in the Northern Hemisphere.

This last result suggests that if the data coverage were more uniform, we would expect few differences to exist between the Southern and Northern hemispheres. This is investigated in the next section, where wind obser-

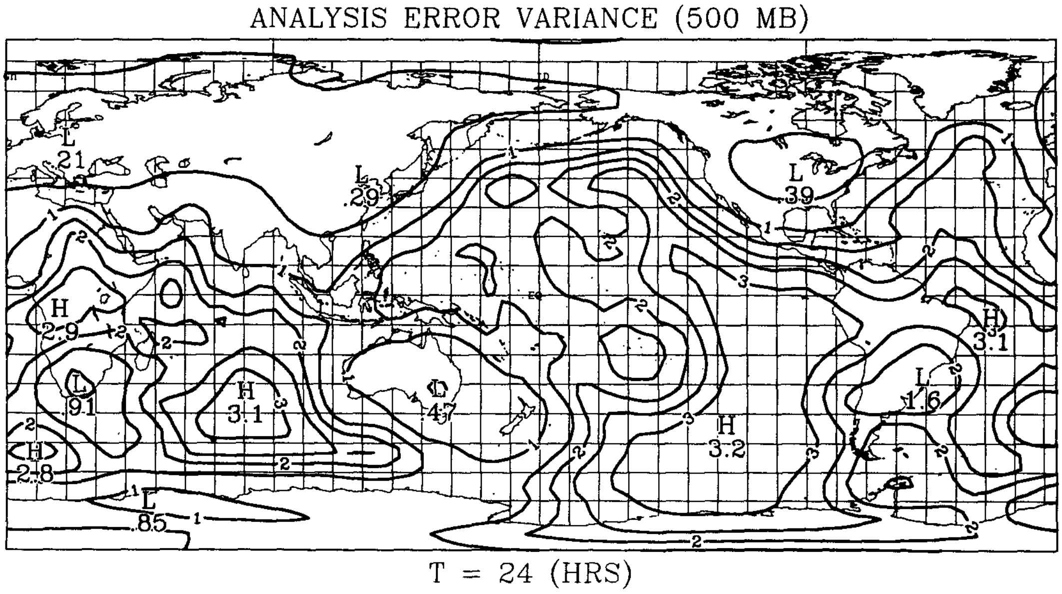

FIG. 5. Analysis error variance at the final time for an assimilation without the time integration of the forecast error covariances. A contour interval of 0.5×10^{-12} s^{-2} has been used.

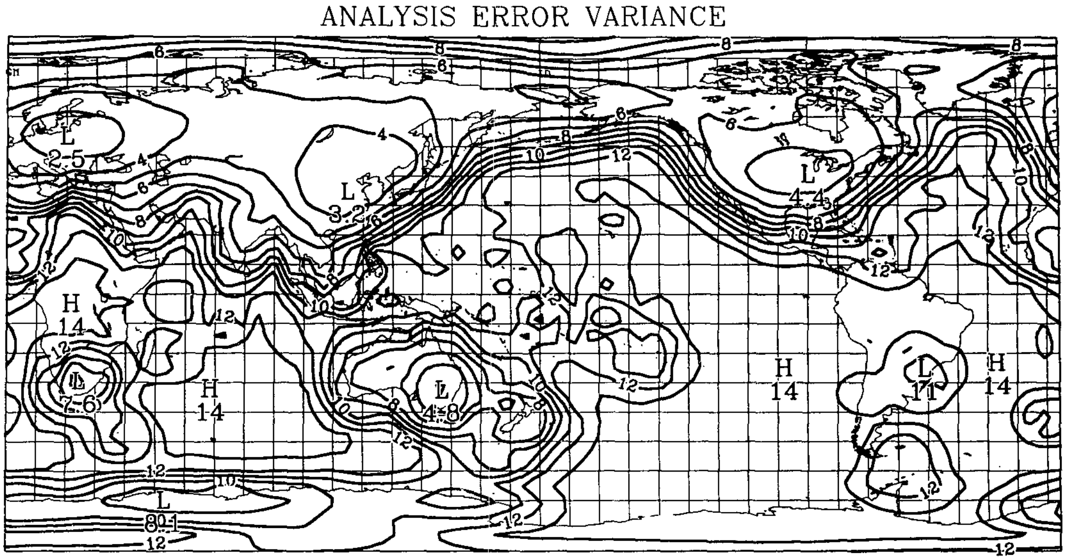
ANALYSIS ERROR VARIANCE

A) T = 0 (HRS)

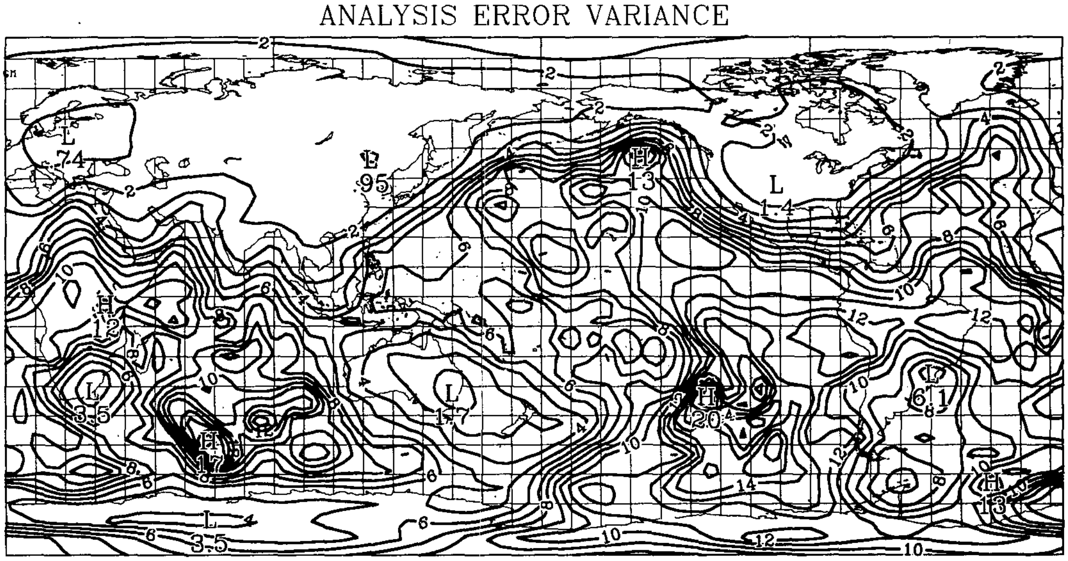
ANALYSIS ERROR VARIANCE

B) T = 24 (HRS)

FIG. 6. As in Fig. 3 but for a characteristic length of the first-guess error of 400 km: (a) at the initial time and (b) at the final time.

vations coming from a simulated satellite-based lidar system are added to the radiosonde network.

5. Experiments with Doppler wind data from a satellite-based lidar instrument

In recent years, both NASA and the European Space Agency have proposed to launch a satellite-based Doppler lidar instrument that would provide a fairly global coverage of radial wind measurements along the line of sight (Curran 1987, 1989; Baker 1991; Betout et al. 1989). Figure 8 shows the data coverage associated with polar orbits at altitudes of 400 km (Fig. 8a) and 800 km (Fig. 8b). This particular choice is dictated by the fact that below 400 km the orbit is unstable, while at 800 km the lidar instrument is becoming less accurate. In both cases, the conical scan has a 45° aperture. The main feature emerging from Fig. 8 is that when orbiting at 400 km, there are significantly larger data gaps than those created when on

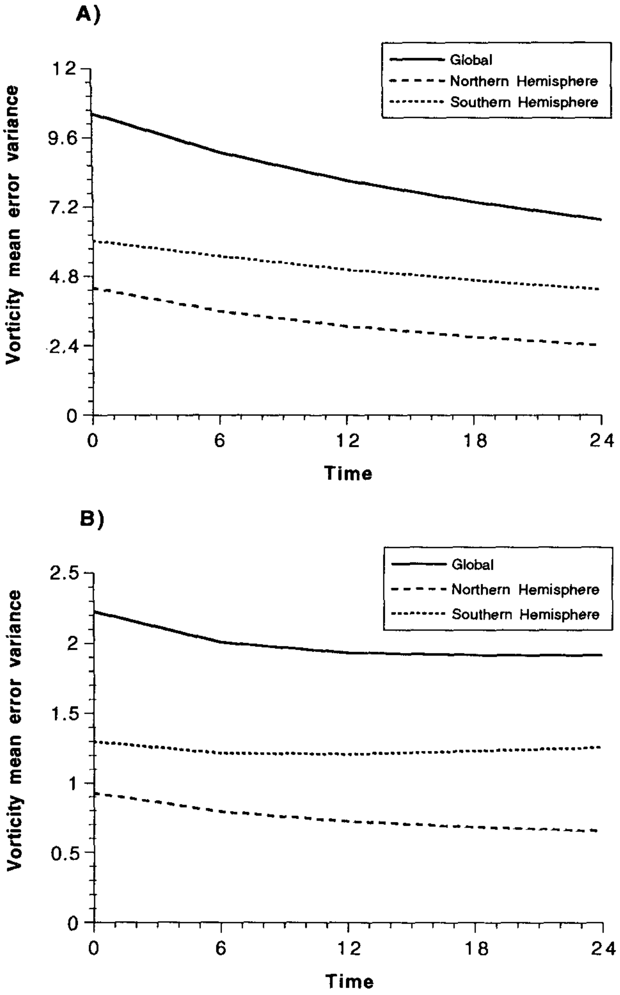

FIG. 7. Time evolution of the global mean analysis error variance (solid line) for a characteristic length of the first-guess error of (a) 400 km and (b) 1200 km. In both figures, the contributions from the Northern and Southern hemispheres have been plotted separately to emphasize the differences existing between the two hemispheres.

an 800-km orbit. Since the lidar instrument provides a measurement over a volume of air that is very small when compared with the resolution of the model, the observation error must therefore include, on top of the measurement error, wind fluctuations on the unresolved scales. Here, these fluctuations have been estimated to correspond to the radiosonde wind error. Finally, the measurement error made by the instrument has been estimated to be of 1 m s^{-1} for a 400-km orbit and 4.3 m s^{-1} when orbiting at 800 km due to a deterioration in the signal-to-noise ratio.

The Doppler wind lidar data used here consist of a single wind component measured along the direction of the line of sight; the orbitography simulator provided the location of the measurement and the direction of the line of sight that were used in the simulation and assimilation of the data. In all the following experiments, the methodology is the same as in the previous section, but now, Doppler wind lidar data have been simulated and added on top of the same radiosonde data used in the preceding section. (The same initial condition situations were used to simulate the data.) The lidar data are inserted at every hour, while the

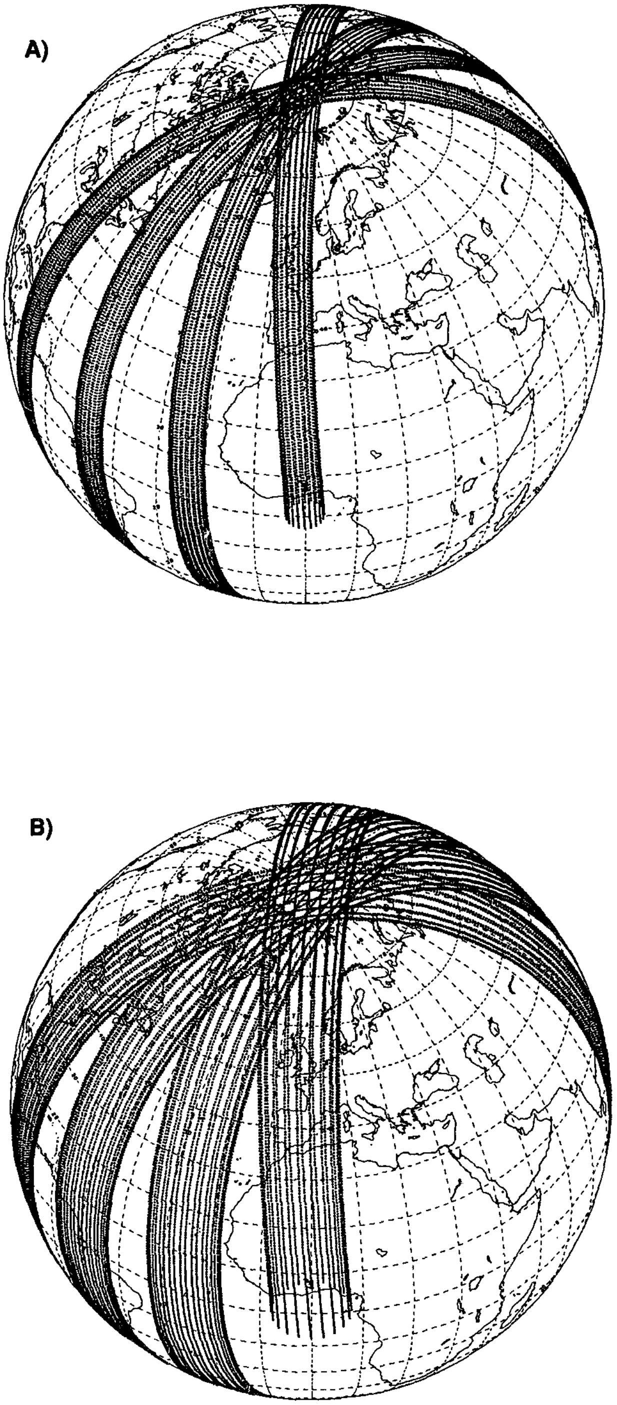

FIG. 8. Typical data coverage for a satellite on a polar orbit at an altitude of (a) 400 km and (b) 800 km. Distribution of the points corresponds to those of a conical scan with a scanning period of 10 s. The shot frequency was set to 2 Hz.

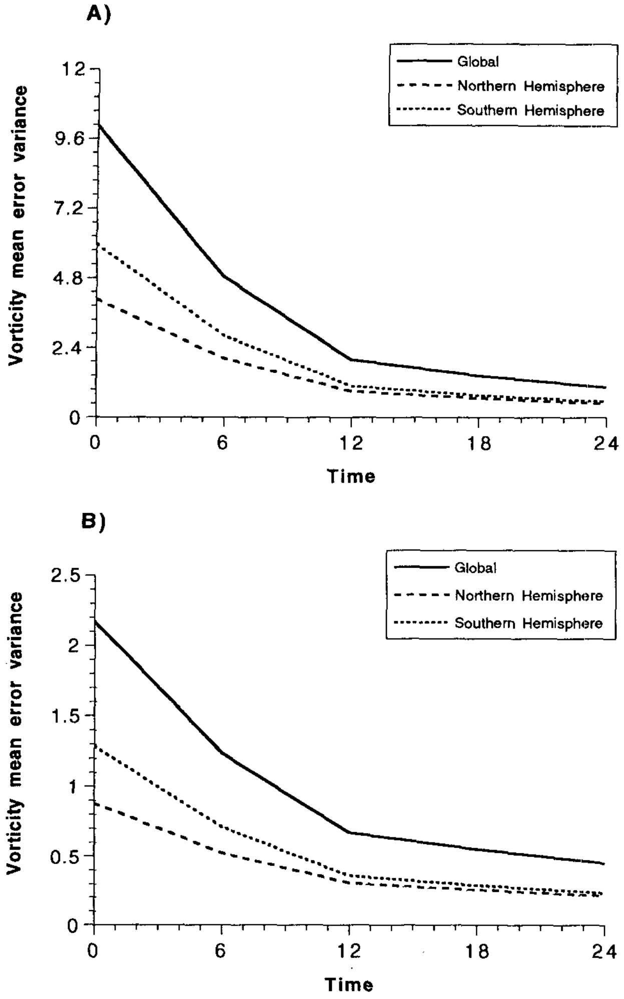

FIG. 9. As in Fig. 7 but for an assimilation using the Lidar data coming from a satellite on a polar orbit at an altitude of 400 km. Results are shown for two experiments using a characteristic length of the first-guess error of (a) 400 km and (b) 1200 km.

radiosonde network comes in at every 6 h, as before. In the first experiment, the satellite is on a polar orbit at an altitude of 400 km, and the lidar shots have a 1-Hz firing frequency (3600 wind measurements per hour): an observation error of 2.45 m s^{-1} on the radial wind component has been considered. Over a 24-h period, the volume of data corresponds to 86 400 single wind component observations that must be added to the 10 845 scalar observations of the radiosonde network. Figure 9 summarizes the results from two experiments that were run by initializing $\mathbf{P}_0^f$ with a forecast error scale of 400 km (Fig. 9a) and 1200 km (Fig. 9b). A comparison with Fig. 7 shows that the lidar data have a very beneficial impact on the quality of the analysis. After 24 h, the data coverage being then nearly uniform, the quality of the analysis in the Southern Hemisphere is now comparable with that of the Northern Hemisphere. These experiments were repeated for an 800-km orbit, and Fig. 10 shows the mean error variance. Although a qualitatively similar error reduction is observed, the increase in the measurement error has a detrimental effect that overcomes the beneficial effect of having a more global data coverage. For instance, for an initial forecast error correlation scale of 1200 km, the mean error variance $\bar{\sigma}^2$ at the end of the assimilation period is found to be $\bar{\sigma}^2 = 0.45 \times 10^{-12}$ s^{-2} for the 400-km orbit, while it goes up to 0.81×10^{-12} s^{-2} for a satellite orbiting at an altitude of 800 km. Both cases converge to an error level that is lower than the variance of 1.915×10^{-12} s^{-2} obtained with the radiosonde data alone. For a forecast error correlation scale of 400 km, the variance level rises but the 400-km orbit still yields a more accurate analysis. Figure 11 shows the corresponding analysis error variance field at $t = 24$ h for the 400-km orbit (Fig. 11a) and the 800-km one (Fig. 11b). By providing measurements in regions where none are available from the radiosonde network, the lidar data can put a stop to the unlimited error growth observed in the previous experiments. The impact of the nonglobal data coverage of the 400-km altitude orbit is now clearly visible

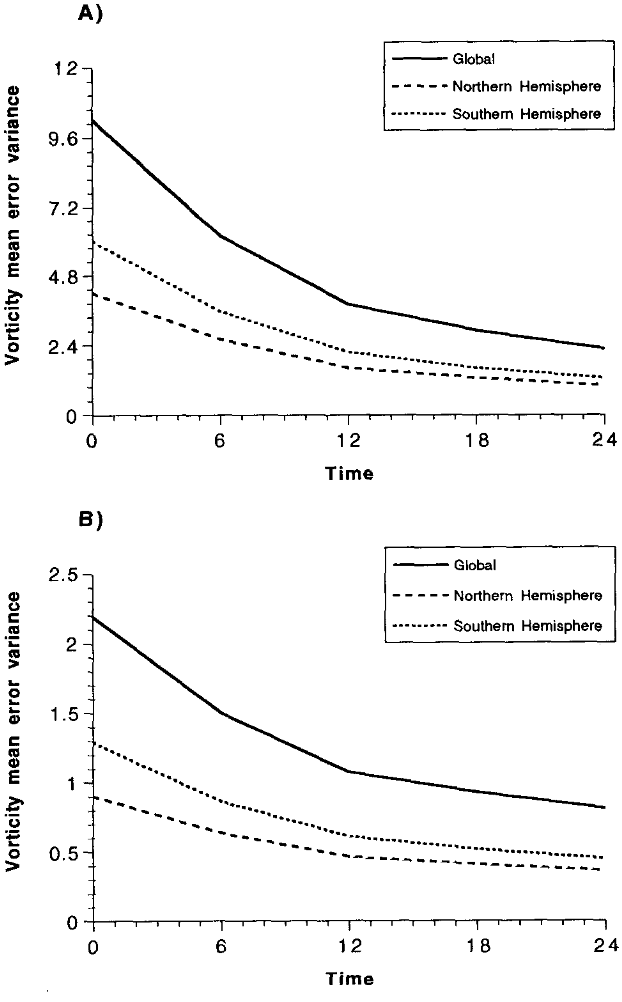

FIG. 10. Same as Fig. 9 but for a satellite at an altitude of 800 km.

A) ALT.: 400 KM

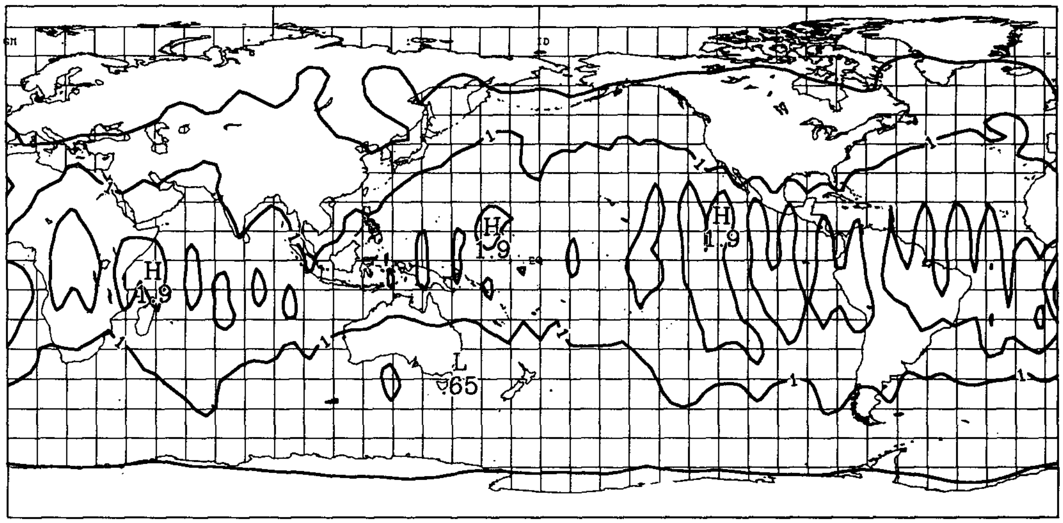

T = 24 (HRS)

B) ALT.: 800 KM

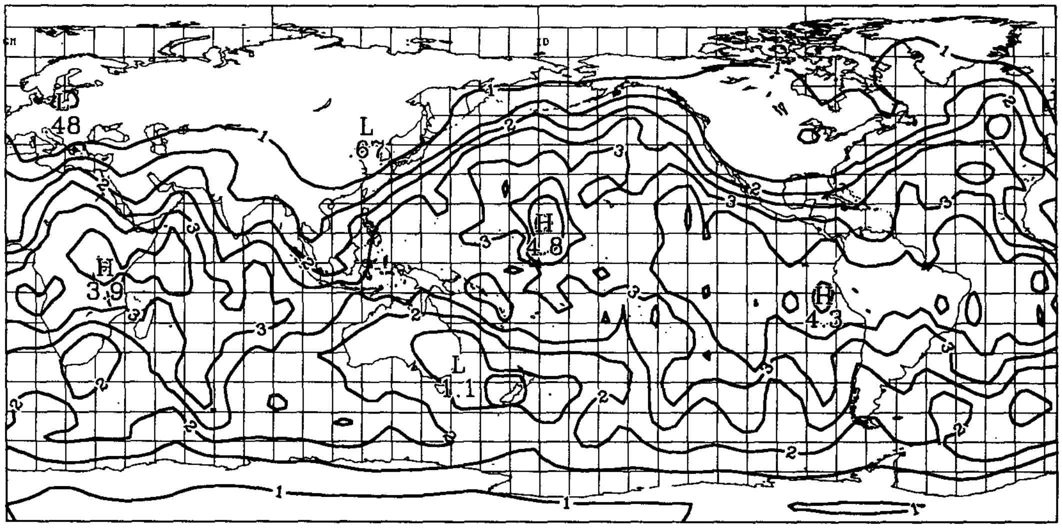

T = 24 (HRS)

FIG. 11. Analysis error variance field at t = 24 h for an assimilation using Lidar data obtained from a satellite at an altitude of (a) 400 km and (b) 800 km. In both cases, a characteristic length of the first-guess error of 400 km has been used. A contour interval of 0.5×10^{-12} s^{-2} has been used.

in the tropical belt as an alternation of high and low values in the vorticity error variance field. Finally, it is also worth noticing that in both cases the error variance is higher in the equatorial region; this is a consequence of having a higher number of lidar measurements in the polar regions. This would suggest that shot management schemes should be designed so as to provide a more uniform coverage by reducing the number on shots in the polar regions and increasing it in the equatorial region.

6. Conclusions

The most striking feature of the results obtained with the tangent linear model is the impact of instability processes on the dynamics of error growth, which is most pronounced in regions of data voids. In these regions, forecast errors may exceed by far those predicted by optimal interpolation. The results that were presented here point to the fact that local error growth is related to the presence of strong vorticity gradients that are characteristic of shear flow instabilities. This suggests that if the EKF was based on a more complex model, other types of instabilities (e.g., baroclinic instability) are likely to lead also to error growth. In experiments with a linear Kalman filter where the linear flow does not support any instability mechanism, error growth stems from an external model error forcing (Dee 1991). In the present study, no model error was considered to emphasize that error growth could occur even in its absence. But it must be kept in mind that a consequence of having no model error is that it usually produces overly optimistic results.

Although the methodology adopted here is correct for a study of the large-scale part of a flow over a 24-h period, the impact of having chosen the true state for the initial estimate of the atmospheric state could be questioned if the assimilation was to be carried out over a period that exceeds that over which the tangent linear model is valid. This limit of validity is determined by comparing the error obtained with the full nonlinear model against the one predicted by the tangent linear model when the initial error is of an amplitude corresponding to the estimate used for the initial error covariance. For longer time periods, the evolution of the forecast error covariance should be determined by integrating the EKF with an initial estimate of the model state that contains an error level consistent with the initial assumption made on its error covariance; this would be the next step.

Finally, the EKF is a very useful tool to perform OSSEs since it provides not only an analysis but also information on its accuracy. In this paper, a mini-OSSE was conducted to make a preliminary assessment of the impact of data coming from a proposed satellite-based Doppler wind lidar instrument. Our results have shown that the availability of a global coverage of wind observations is able to put a stop to the unlimited error growth that was observed when only radiosonde data were used. The impact is even more important in the Southern Hemisphere, which is poorly covered by the radiosonde network. Two scenarios have been investigated for 400- and 800-km orbits. It was concluded that, due to a loss in the measurement accuracy, the 800-km orbit gives a less accurate analysis even though the data coverage was more global.

Acknowledgments. The authors would like to thank Philippe Veyre of Météo-France, who contributed to the development of the computer code, and Alain Dabas of the Laboratoire de Météorologie Dynamique in Palaiseau, France, who provided the program generating the orbitography for the satellite experiments. This work was supported by Contract 8850-90-HGE-I from the European Space Agency.

The first author would like to express his appreciation to the staff of Météo-France for their hospitality during his stay in Paris.

APPENDIX A

The Adjoint of the Forward Interpolation

The availability of the adjoint of $\mathbf{H}$ can be used to reduce the number of interpolations that must be performed to obtain an explicit form for it. The adjoint being defined in relation to a given inner product, consider E to be the spectral space of dimension N (the model state) and O, the observation space of dimension M; their respective inner products are taken to be

$$\langle \mathbf{f}, \mathbf{g} \rangle_E = \mathbf{f}^{\mathrm{T}}\mathbf{g}, \quad \langle \mathbf{x}, \mathbf{y} \rangle_O = \mathbf{x}^{\mathrm{T}}\mathbf{y}. \tag{A.1}$$

In this appendix, $\mathbf{H}$ will stand for what was previously designed by $\mathbf{H}'_k$ and is therefore assumed to be linear. By definition, (A.1) implies that the adjoint of $\mathbf{H}$ is such that $\mathbf{H}^* = \mathbf{H}^{\mathrm{T}}$. Applying the adjoint of the interpolation to the $(M \times M)$ identity matrix will provide an explicit expression for $\mathbf{H}$, and only M adjoint interpolations have to be performed. This can reduce considerably the work required to obtain $\mathbf{H}$ when the number of model variables far exceeds that of the observations to be assimilated.

The adjoint interpolation must, however, be defined in such a way that it can be practically used. For the sake of simplicity, this will be illustrated for observations of vorticity for which $\mathbf{H} = \mathcal{B}\mathcal{S}^{-1}$, that is, an inverse spectral transform of the model state followed by a bilinear interpolation to the observation points. Consider G_1 to be the physical space and $\mathcal{S}: G_1 \rightarrow E$. The inner product on G_1 is so chosen that $\mathcal{S}^{-1}$ is "unitary," which means that

$$\langle \mathcal{S}^{-1}f, \mathcal{S}^{-1}g \rangle_{G_1} \equiv \langle f, g \rangle_E = \frac{1}{S}\iint_S fg\, dS$$

$$\approx \sum_i \frac{(\mathcal{S}^{-1}f)_i(\mathcal{S}^{-1}g)_i\omega_i}{N_i},$$

and the sum is carried over all grid points: ω_i and N_i are the Gaussian weight and the number of grid points on the latitude circle of the grid point, respectively. With this definition, the adjoint of $\mathcal{S}^{-1}$ corresponds to the spectral transform itself [see the discussion in appendix A of Talagrand and Courtier (1987)].

On the other hand, it would be most convenient to consider the inner product for the gridpoint space G_2 to be

$$\langle \mathbf{f}, \mathbf{g} \rangle_{G_2} = \mathbf{f}^{\mathrm{T}}\mathbf{g},$$

in which case

$$\langle \mathbf{Z}, \mathcal{B}\mathbf{Y} \rangle_O = \langle \mathcal{B}^*\mathbf{Z}, \mathbf{Y} \rangle_{G_2},$$

implying immediately that $\mathcal{B}^* = \mathcal{B}^{\mathrm{T}}$. The elements of G_1 and G_2 are thus the same, the values of ζ at the grid points, but G_1 and G_2 nevertheless differ by having distinct inner products.

To get the best of both worlds, it suffices to introduce a supplementary transformation, the identity $\mathbf{I}: G_1 \rightarrow G_2$. At first, this may look trivial but the adjoint of the identity is not and is such that

$$\langle \mathbf{f}, \mathbf{Ig} \rangle_{G_2} = \sum_i f_i g_i = \langle \mathbf{I^*f}, \mathbf{g} \rangle_{G_1} = \sum_i (I^*f)_i g_i \frac{\omega_i}{N_i},$$

and consequently,

$$(I^*f)_i = \frac{N_i}{\omega_i} f_i.$$

The application of $\mathbf{I^*}$ is then achieved by multiplying every grid point by its corresponding weight N_i/ω_i.

The bilinear interpolation of the model variable ζ to an observation point implies that

$$\zeta_m = \alpha_{mi_1}\zeta_{i_1} + \alpha_{mi_2}\zeta_{i_2} + \alpha_{mi_3}\zeta_{i_3} + \alpha_{mi_4}\zeta_{i_4},$$

where the coefficients α_{mi} correspond to the weights assigned by a bilinear interpolation to the values of ζ at the four grid points defining the mesh that contains the observation point. A column of $\mathcal{B}^{\mathrm{T}}$ represents a gridpoint field that contains only zeros except for those four points that take the values of the corresponding weight. Therefore, when $\mathcal{B}^{\mathrm{T}}$ is applied to the mth column of the identity matrix, it produces a gridpoint field that is zero everywhere but at these four points.

The next operation consists of applying the adjoint of the identity $\mathbf{I^*}$ by multiplying each gridpoint value by the proper weight N_i/ω_i. The result from these two operations yields a gridpoint field to which is applied the spectral transform that produces a model state vector that corresponds to the result of applying $\mathbf{H^*}$ to one column of the identity matrix.

APPENDIX B

Spectral Representation of Homogeneous and Isotropic Error Covariances

It is often assumed in the operational practice that the forecast error on the streamfunction ψ has a constant variance and its correlation is homogeneous and isotropic and even Gaussian. This means that the forecast error covariance is expressed as

$$\begin{aligned} P_G^f(Q, Q') &= \mathcal{E}[\psi(Q)\psi(Q')] \\ &= f(r) = \sigma_\psi^2 \exp\left(-\frac{r^2}{2a^2}\right), \end{aligned} \qquad \text{(B.1)}$$

with a the correlation length of the correlation and r the distance between two points Q and Q' on the sphere. An estimate of the error variance σ_ψ^2 can be obtained by taking ψ to be geostrophically related to the geopotential ϕ, in which case

$$\sigma_\psi = \frac{g}{f}\sigma_\phi. \qquad \text{(B.2)}$$

Equation (B.1) expresses the error covariance in physical space, but an expression is needed for it in spectral form. Such an expression has been known for quite some time and can be found, for instance, in Boer (1983). For the sake of completeness, the derivation is recalled here as it has been presented in Courtier (1987).

For the sake of brevity, ψ will stand for the error on the streamfunction and is spectrally expressed as

$$\psi = \sum_{n,m} \tilde{\psi}_n^m Y_n^m.$$

Therefore,

$$\tilde{\psi}_n^m = \frac{1}{4\pi} \iint_S \psi(\lambda, \theta) Y_n^{-m} dS.$$

Introducing the short-hand notation l and m for (m, n) and (m', n'), respectively, an element of the error covariance matrix is then

$$\begin{aligned} P_{l,m}^f &= \mathcal{E}(\tilde{\psi}_n^m \tilde{\psi}_{n'}^{m'}) \\ &= \frac{1}{(4\pi)^2} \mathcal{E}\left[\iint_S \psi(Q) Y_n^{-m} dS \iint_{S'} \psi(Q') Y_{n'}^{-m'} dS'\right] \\ &= \frac{1}{(4\pi)^2} \iint_S \iint_{S'} Y_n^{-m} Y_{n'}^{-m'} \mathcal{E}[\psi(Q)\psi(Q')] dS dS' \\ &= \frac{1}{(4\pi)^2} \iint_S \iint_{S'} Y_n^{-m} Y_{n'}^{-m'} P_G^f dS dS'. \end{aligned} \qquad \text{(B.3)}$$

Spherical coordinates defined with respect to a pole located at point Q are most convenient to expand (B.1) in spherical harmonics because only zonal components are necessary. Hence,

$$P_G^f = \sigma_\psi^2 \exp\left(-\frac{r^2}{2a^2}\right) = \sigma_\psi^2 \sum_p b_p Y_p'^0, \qquad \text{(B.4)}$$

the prime stressing the fact that these harmonics are different. Of course, this argument holds also for any isotropic function $f(r)$. Introducing (B.4) into (B.3) yields

$$P_{l,m}^f = \frac{\sigma_\psi^2}{(4\pi)^2} \iint_S Y_n^{-m} dS \sum_p b_p \left(\iint_{S'} Y_p'^0 Y_{n'}^{-m'} dS'\right). \qquad \text{(B.5)}$$

It can be shown that if $m' = 0$, then

$$\iint_{S'} Y_p'^0 Y_{n'}^{-m'} dS' = C_{m'} \frac{4\pi}{(2n+1)^{1/2}} Y_{n'}^{m'}(Q) \delta_{p=n'},$$

where $C_{m'} = 1$ if $m' = 0$ and $C_{m'} = 1/2$ when $m' \neq 0$. The proof of this is somewhat technical and can be found elsewhere (see, e.g., Hobson 1931). With this, one finally gets

$$P^f_{l,m} = \sigma_\psi^2 \frac{b_n}{(2n+1)^{1/2}} C_m \delta_{n=n'} \delta_{m=m'}, \quad \text{(B.6)}$$

which is seen to be a diagonal matrix.

Once the spectral covariances for the streamfunction are known, it is straightforward to show that since

$$\tilde{\zeta}_n^m = -\frac{n(n+1)}{R^2} \tilde{\psi}_n^m,$$

then

$$P^f_{l,m}(\zeta) = \sigma_\psi^2 \frac{b_n}{(2n+1)^{1/2}} \frac{n^2(n+1)^2}{R^4} C_m \delta_{n=n'} \delta_{m=m'},$$

R being the radius of the earth.

REFERENCES

Baker, W. E., 1991: Science advances anticipated with the laser atmospheric wind sounder. *Technical Digest on Coherent Laser Radar: Technology and Applications,* Vol. 12, Optical Society of America, 234–237.

Bartello, P., and H. L. Mitchell, 1992: A continuous three-dimensional model of short-range forecast error covariances. *Tellus,* **44A,** 217–235.

Bélanger, P. R., 1974: Estimation of noise covariance matrices for a linear time-varying stochastic process. *Automatica,* **10,** 267–275.

Betout, P., D. Burridge, and Ch. Werner, 1989: Doppler Lidar Working Group Report. ESA Publications Division, Noordwijk, the Netherlands, 45 pp.

Boer, G. J., 1983: Homogeneous and isotropic turbulence on the sphere. *J. Atmos. Sci.,* **40,** 154–163.

Brown, R. G., 1983: *Introduction to Random Signal Analysis and Kalman Filtering.* John Wiley & Sons, 347 pp.

Cohn, S. E., and D. F. Parrish, 1991: The behavior of forecast error covariances for a Kalman filter in two dimensions. *Mon. Wea. Rev.,* **119,** 1757–1785.

Courtier, P., 1987: Application du contrôle optimal à la prévision numérique en météorologie. Ph.D. thesis, Université Pierre et Marie Curie (Paris VI), Paris, France, 252 pp.

——, and O. Talagrand, 1987: Variational assimilation of meteorological observations with the adjoint vorticity equation. II: Numerical results. *Quart. J. Roy. Meteor. Soc.,* **113,** 1329–1347.

——, and J.-F. Geleyn, 1988: A global numerical weather prediction model with variable resolution: Application to the shallow-water equations. *Quart. J. Roy. Meteor. Soc.,* **114,** 1321–1346.

——, and O. Talagrand, 1990: Variational assimilation of meteorological observations with the direct and adjoint shallow-water equations. *Tellus,* **42A,** 531–549.

Curran, R. J., 1987: LAWS instrument panel report. Volume IIg of NASA's series on Earth observing system, Washington, D.C., 55 pp.

——, 1989: NASA's plans to observe the Earth's atmosphere with Lidar. *IEEE Trans. Geosci. Remote Sens.,* **27,** 154–163.

Daley, R., 1991: *Atmospheric Data Analysis.* Cambridge University Press, 457 pp.

——, 1992: The lagged innovation covariance: A performance diagnostic for atmospheric data assimilation. *Mon. Wea. Rev.,* **120,** 178–196.

Dee, D. P., 1991: Simplification of the Kalman filter for meteorological data assimilation. *Quart. J. Roy. Meteor. Soc.,* **117,** 365–384.

——, S. E. Cohn, A. Dalcher, and M. Ghil, 1985: An efficient algorithm for estimating noise covariances in distributed systems. *IEEE Trans. Autom. Control,* **AC-30,** 1057–1065.

Derber, J. C., D. F. Parrish, and S. J. Lord, 1991: The new global operational analysis system at the National Meteorological Center. *Wea. Forecasting,* **6,** 538–547.

Ghil, M., 1989: Meteorological data assimilation for oceanographers. Part I: Description and theoretical framework. *Dyn. Atmos. Oceans,* **13,** 171–218.

——, S. Cohn, J. Tavantzis, K. Bube, and E. Isaacson, 1981: Application of estimation theory to numerical weather prediction. *Dynamic Meteorology: Data Assimilation Methods.* L. Bengtsson, M. Ghil, and E. Källén, Eds., Springer-Verlag, 330 pp.

Hobson, E. W., 1931: *The Theory of Spherical and Ellipsoidal Harmonics.* Cambridge University Press, 500 pp.

Hollingsworth, A., and P. Lönnberg, 1986: The statistical structure of short-range forecast errors as determined from radiosonde data. Part I: The wind field. *Tellus,* **38A,** 111–136.

Jazwinski, A., 1970: *Stochastic Processes and Filtering Theory.* Academic Press, 376 pp.

Kalman, R. E., 1960: A new approach to linear filtering and prediction problems. *Trans. ASME, J. Basic Eng.,* **83D,** 35–45.

——, and R. S. Bucy, 1961: New results in linear filtering and prediction theory. *Trans. ASME, J. Basic Eng.,* **83D,** 95–108.

Lacarra, J. F., and O. Talagrand, 1988: Short-range evolution of small perturbations in a barotropic model. *Tellus,* **40A,** 81–95.

Le Dimet, F. X., and O. Talagrand, 1986: Variational algorithms for analysis and assimilation of meteorological observations: Theoretical aspects. *Tellus,* **38A,** 97–110.

Lorenc, A. C., 1986: Analysis methods for numerical weather prediction. *Quart. J. Roy. Meteor. Soc.,* **112,** 1177–1194.

——, 1988: Optimal nonlinear objective analysis. *Quart. J. Roy. Meteor. Soc.,* **114,** 205–240.

Miller, R. N., and M. Ghil, 1990: Data assimilation in strongly nonlinear currents. *Proc. of the WMO Int. Symp. on Assimilation of Observations in Meteorology and Oceanography,* Clermont-Ferrand, France, WMO, 93–98.

Pailleux, J., 1990: A global variational assimilation scheme and its application for using TOVS radiances. Preprints, *WMO Int. Symp. on Assimilation of Observations in Meteorology and Oceanography.* Clermont-Ferrand, France, WMO, 325–328.

Parrish, D. F., and J. C. Derber, 1992: The National Meteorological Center's spectral statistical-interpolation analysis system. *Mon. Wea. Rev.,* **120,** 1747–1763.

Phillips, N. A., 1986: The spatial statistics of random geostrophic modes and first-guess errors. *Tellus,* **38A,** 314–332.

Rabier, F., and P. Courtier, 1992: 4D assimilation in the presence of baroclinic instability. *Quart. J. Roy. Meteor. Soc.,* **118,** 649–672.

Talagrand, O., and P. Courtier, 1987: Variational assimilation of meteorological observations with the adjoint vorticity equation. I: Theory. *Quart. J. Roy. Meteor. Soc.,* **113,** 1311–1328.

Thépaut, J.-N., and P. Courtier, 1991: Four-dimensional data assimilation using the adjoint of a multilevel primitive equation model. *Quart. J. Roy. Meteor. Soc.,* **117,** 1225–1254.

Vukicewic, T., 1991: Nonlinear and linear evolution of initial forecast errors. *Mon. Wea. Rev.,* **119,** 1602–1611.